Optical Materials 162 (2025) 116841

Contents lists available at ScienceDirect

Optical Materials

journal homepage: www.elsevier.com/locate/optmat

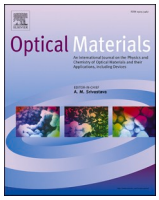

Research Article

A comprehensive exploration of optical properties of $GdAlO_3$: Cr^{3+}

H. Souissi [a,*], S. Kammoun [a], E. Dhahri [a], J. Pina [b], B.F.O. Costa [c], A.L.B. Brito [b], R. Fausto [b,d]

[a] Applied Physics Laboratory, Faculty of Sciences, Sfax University, BP 1171, 3000, Sfax, Tunisia
[b] University of Coimbra, CQC-IMS, Chemistry Department, 3004-535, Coimbra, Portugal
[c] University of Coimbra, CFisUC, Physics Department, 3004-516, Coimbra, Portugal
[d] Spectroscopy@IKU, Faculty of Sciences and Letters, Department of Physics, Istanbul Kultur University, Ataköy Campus, Bakırköy 34156, Istanbul, Türkiye

ARTICLE INFO

Keywords:
UV/Vis.
PLE and PL spectra
Crystal and ligand fields
Transition metal compounds
$GdAlO_3$ perovskite
Photoluminescence

ABSTRACT

This study focused on the optical properties of the Cr^{3+}-doped $GdAlO_3$ perovskite, through comprehensive analysis of its photoluminescence spectra. The $GdAlO_3$: Cr^{3+} perovskite, synthesized by a traditional solid-state process, crystallizes in the orthorhombic *Pbnm* space group, with Cr^{3+} ions substituting Al^{3+} ions in octahedral sites. Photoluminescence excitation and emission spectra of the material were obtained and assigned. The zero-phonon lines ZPL of the observed emission and excitation transitions associated with the Cr^{3+} ions, in the visible range, were determined, and the experimental spectral data were modelled by the Fourier transformation of the autocorrelation function, enabling the calculation of diabatic potential energy profiles for the ground and lowest energy excited states. Crystal field parameters were derived, providing insight into the electronic structure of Cr^{3+} in the O_h symmetry site. The results highlighted the significant impact of coordination on the electronic structure of Cr^{3+} ions, with a notably high nephelauxetic effect parameter ($h = 1.44$), indicating a high degree of covalency in the metal-ligand bonds. Energy transfer from Gd^{3+} to Cr^{3+} in $GdAlO_3$: Cr^{3+} was found to be significant, contributing to the enhancement of the deep-red emission of the compound attributed to the $^2E_g(^2G) \rightarrow {}^4A_{2g}(^4F)$ d-d transition of Cr^{3+}. Finally, the CIE 1931 chromaticity coordinates of the photoluminescence emission of $GdAlO_3$:Cr^{3+} were determined, positioning the emission at the boundary of the chromaticity diagram, indicative of its high color purity and potential suitability for red light-emitting display applications.

1. Introduction

Gadolinium aluminum oxide ($GdAlO_3$) has gained significant attention across various scientific fields due to its versatile properties [1–5]. Its perovskite-like crystal structure imparts this material exceptional thermal stability, mechanical strength, and optical transparency, making it a promising candidate for diverse technological applications. The material's versatility is further enhanced by the ability to fine-tune its properties through doping and alloying [5–10]. In optoelectronics, $GdAlO_3$ is particularly valued for its wide bandgap, excellent optical transparency, and compatibility with semiconductor materials, making it ideal for light-emitting diodes (LEDs), photodetectors, and solar cells [1–5].

Recent research has focused on Cr^{3+} doping in $GdAlO_3$, revealing significant potential for tailoring the material's optical and magnetic properties [4,5,11]. Chromium ions introduce a range of functionalities, from photoluminescence to magnetism, thereby expanding the applications of $GdAlO_3$ across multiple disciplines. In biomedical engineering, Cr^{3+}- doped $GdAlO_3$ shows promise for dual-mode imaging and therapeutic applications. The combined optical and magnetic properties enable advanced imaging techniques like fluorescence and magnetic resonance imaging (MRI), offering enhanced contrast and spatial resolution. Additionally, the potential to functionalize Cr^{3+}- doped $GdAlO_3$ nanoparticles for targeted drug delivery positions this material as a candidate for precision medicine and the ranostic applications.

In this manuscript, we present a comprehensive investigation of Cr^{3+} doping within $GdAlO_3$, covering synthesis of the material and in-depth analysis of its optical properties through investigation of its photoluminescence spectra. By elucidating the fundamental mechanisms underlying the optical properties of Cr^{3+}- doped $GdAlO_3$, we aim to inspire further research and innovation in harnessing the potential of dopant-engineered complex oxides for advanced materials and technologies.

* Corresponding author.
E-mail address: souissi.hajer.fss@gmail.com (H. Souissi).

https://doi.org/10.1016/j.optmat.2025.116841
Received 28 November 2024; Received in revised form 15 February 2025; Accepted 18 February 2025
Available online 19 February 2025

2. Experimental

For the synthesis of $GdAlO_3$: Cr, high-purity gadolinium oxide Gd_2O_3, aluminum oxide Al_2O_3, and chromium oxide Cr_2O_3 powders were used. The solid-state method employed offers a straight forward and effective route for producing $GdAlO_3$: Cr, allowing for precise control over the reaction conditions to achieve the desired phase purity and properties. First, the powders were annealed at 700 °C, followed by thorough grinding to ensure uniform mixing of the reactants. The mixture was then gradually heated to 1200 °C for sintering, resulting in formation of $GdAlO_3$: Cr. The sintered powder was then compressed into pellets with an 8 mm diameter, for analyses by X-ray powder diffraction (XRD) and ultraviolet–visible (UV/Vis) photoluminescence excitation (PLE) and emission (PL) spectroscopies.

In the XRD experiments, an X-Ray Siemens D5000 powder diffractometer was used. CuKα radiation (λ = 1.5406 Å) was employed, with the data collection covering a 2θ range of 20°–100° with a step size of 0.02°. Photoluminescence measurements were performed on a Horiba-Jobin-Yvon Fluorolog 322 spectrometerin time-resolved mode, using a pulsed lamp with a 0.05 ms delay after flash.

3. Results and discussion

3.1. Powder X-ray diffraction

Fig. 1 depicts the X-ray powder diffraction pattern of the synthesized $GdAlO_3$: Cr sample. Comparison of the samples' XRD profile with reference data of the International Centre for Diffraction Data (ICDD) XRD database (previous Joint Committee on Powder Diffraction Standards database, JCPDS), allowed to conclude that the obtained diffraction peaks correspond to those characteristics of the $GdAlO_3$ orthorhombic perovskite structure phase, *Pbnm* space group (JCPDS 46–0395) (Fig. 2). It has been shown before that, in Cr^{3+}-doped $GdAlO_3$, the Cr^{3+} ions predominantly replace Al^{3+} [12–15], which occupies an octahedral coordination site (O_h site symmetry), with six O^{2-} closest neighbors.

3.2. Material's optical properties

3.2.1. PLE and PL spectra

Fig. 3 shows the room temperature photoluminescence excitation (PLE) spectra of the synthesized $GdAlO_3$: Cr^{3+} sample. The PLE spectrum obtained with emission at λ_{em} = 697 nm and collected in the range 200–700 nm range was found to be in good agreement with those previously reported [1,17,18]. In the UV region, the PLE spectrum presents two narrow bands assigned to Gd^{3+} 4f-4f transitions: an intense band at

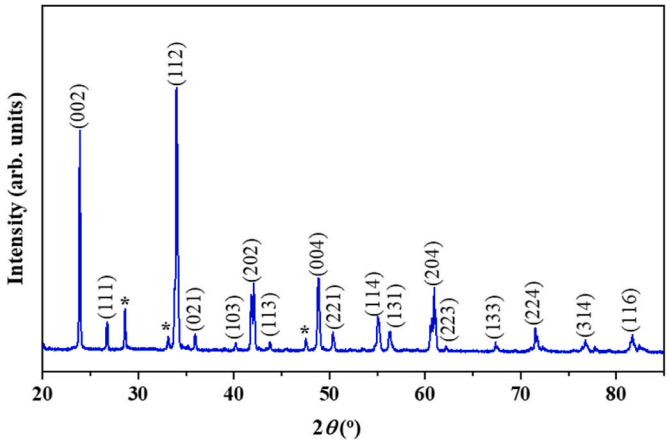

Fig. 1. Powder XRD pattern of the synthesized $GdAlO_3$:Cr^{3+} perovskite. Bands marked with * are due to Gd_2O_3 impurity.

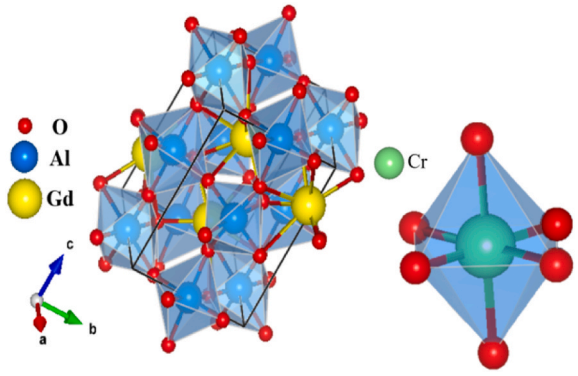

Fig. 2. Unit cell of $GdAlO_3$(as drawn with the Vesta software [16]) and a representation of the [CrO_6] octahedron in the doped material, with the Cr^{3+} ion occupying a site of O_h symmetry. The $GdAlO_3$ crystal data was obtained from [2].

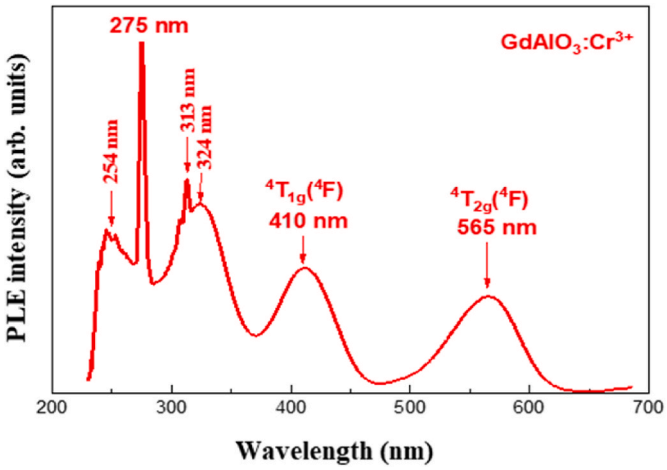

Fig. 3. Room temperature PLE spectrum of the synthesized $GdAlO_3$:Cr^{3+} sample, monitored at λ_{em} = 697 nm.

275 nm, ascribed to the $^8S_{7/2} \rightarrow {}^6I_{11/2}$ transition, and a lower intensity band located at 313 nm and assigned to the $^8S_{7/2} \rightarrow {}^6P_{7/2}$ transition. The broad band with maximum at 324 nm is attributed to Gd^{3+} 4f-4f transitions from ground state $^8S_{7/2}$ to excited states ^6P_j. On the other hand, the two PLE broad bands observed in the visible region, with maxima at 410 and 565 nm, are attributed to the Cr^{3+} 3d-3d transitions, from the $^4A_{2g}(^4F)$ ground state to the $^4T_{1g}(^4F)$ and $^4T_{2g}(^4F)$ excited states, respectively. The Cr^{3+} ion is also in the origin of the UV band at 254 nm, assigned to the spin-allowed Cr^{3+} inner transitions from the $^4A_{2g}(^4F)$ ground state to the $^4T_{1g}(^4P)$ excited state and to charge transfer (CT) involving electron transfer from the Cr^{3+} ions to the conduction band [1].

Fig. 4 presents the room temperature photoluminescence emission (PL) spectra of the studied material under 377 nm excitation, compared to that of the undoped $GdAlO_3$ obtained using the same experimental conditions. In the spectrum of the Cr^{3+}-doped material, a well-resolved, strong band is observed at 726 nm that is absent in the spectrum of the pristine $GdAlO_3$. This band is assigned to the emission from the first excited state of Cr^{3+} $^2E_g(^2G) \rightarrow {}^4A_{2g}(^4F)$ ground state. This strong deep-red emission has great potential for application in various domains, including optoelectronic devices, and, in particular, fluorescent nanoprobes for in vivoimaging [19].

The PL band at 735 nm is related with the energy transfer between isolated Cr^{3+} ions and exchange-coupled Cr^{3+} pairs formed by Cr^{3+} ions occupying adjacent lattice sites. This type of band has been detected in

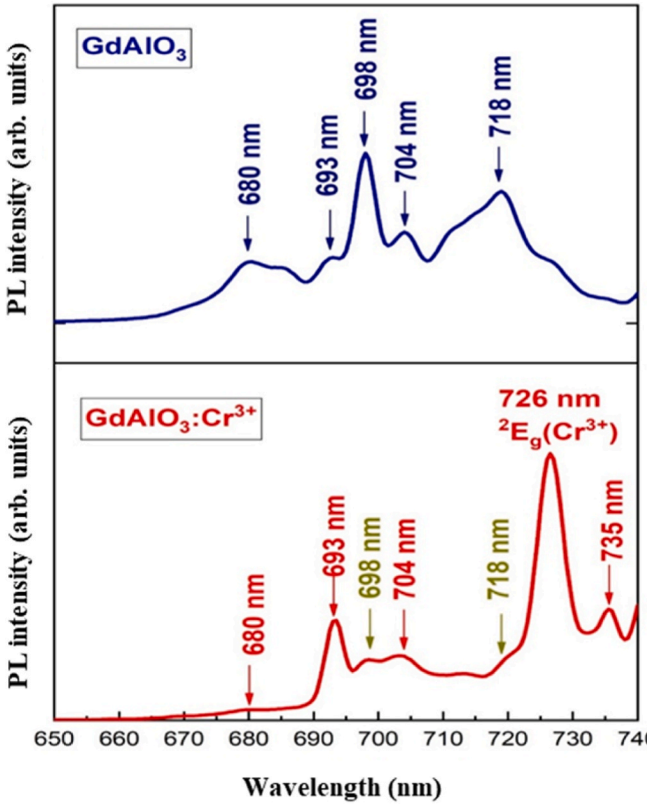

Fig. 4. Room temperature PL spectrum (650–740 nm range) of the investigated $GdAlO_3$:Cr^{3+} sample, obtained under 377 nm excitation, compared to that of the pure $GdAlO_3$.

the PL spectra of different Cr^{3+}-doped materials, such as $GaAlO_3$:Cr^{3+} and $LaAlO_3$:Cr^{3+} [1]. The bands at 680, 698, 704 and 718 nm are ascribable to the $^6P_j \rightarrow {}^8S_{7/2}$ transitions of Gd^{3+} ions [20].

In coordination systems with an inversion symmetry center, vibronic coupling is an efficient way to raise electron-dipole intensity during d-d transitions. Configurational-coordinate analysis within the Franck-Condon model, allows to estimate the zero-phonon line (ZPL) emission and excitation energies of the Cr^{3+} ions in the O_h symmetry site from the PL and PLE spectra. The $E(^4T_{2g}(^4F))_{ZPL}$ and $E(^4T_{1g}(^4F))_{ZPL}$ excited states' energies can be accurately determined from the experimental PLE spectrum, while the $E(^2E_g(^2G))_{ZPL}$ excited state energy can be obtained from the PL spectrum.

The auto correlation function $\langle\varphi|\varphi(t)\rangle$ (which is the overlap of $\varphi(t=0)$ with $\varphi(t)$, φ being the time-dependent wave function of the system) was used in the modeling of the PLE spectrum shown in Fig. 3 accounting for the vibronic coupling (Fig. 5).

The autocorrelation function shows the wave function's dynamic progression from the initial state to the end state within a potential energy well. The absorption spectrum is obtained from the Fourier transformation of the autocorrelation function [21–25], according to:

$$I(\omega) = C\omega^3 \int_{-\infty}^{+\infty} e^{i\omega t} \left\{ \langle\langle\varphi|\varphi(t)\rangle\rangle e^{-\Gamma^2 t^2 + i\frac{E_{ZPL}}{\hbar}t} \right\} dt \quad (1)$$

where the energy of the origin (ZPL energy) is denoted as E_{ZPL}, ω is the absorption frequency, C a constant, and the phenomenological damping factor Γ controls the width of each line in the spectrum. Wavenumber units are used for all amounts.

The evaluation of the autocorrelation function is facilitated by assuming (i) that the potential energy wells are harmonic and the force constants are identical for the initial and final states, (ii) that the transition dipole moment is constant, and (iii) that the normal coordinates of the two states are identical. In this case, the autocorrelation equation takes the following analytical form [24,25]:

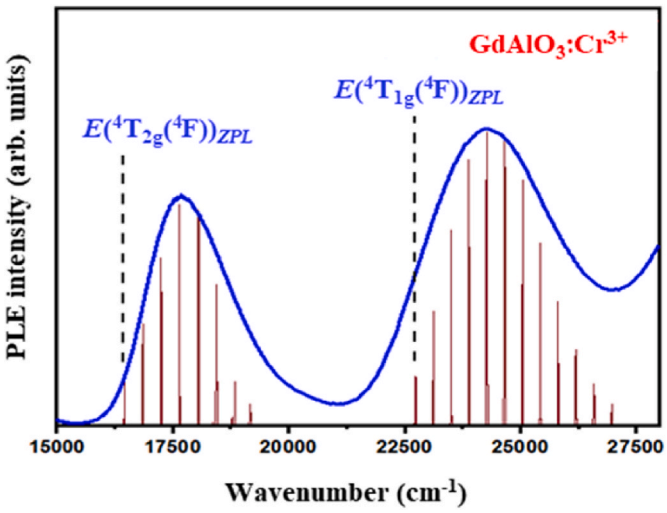

Fig. 5. The modeling of the Cr^{3+} d-d related features observed in the PLE spectrum of the $GdAlO_3$: Cr^{3+} phosphor in the visible region. The black dashed lines indicate the positions of the excited-state ZPL energies, $E(^4T_{2g}(^4F))_{ZPL}$ and $E(^4T_{1g}(^4F))_{ZPL}$; the vibrational progressions are shown in brown.

$$\langle\varphi|\varphi(t)\rangle = \exp\left(\sum_j \left[-\frac{\Delta Q_j^2}{2}\left(1 - e^{ik_j t}\right) - \frac{ik_j t}{2} \right]\right) \quad (2)$$

where the vibrational frequencies of each mode and the displacement along the normal coordinate Q_j are denoted by k_j and ΔQ_j respectively. A frequency of 484 cm^{-1} was considered for k, which corresponds to the frequency of $GdAlO_3$ for the Raman active mode of e_g symmetry [13].

Raman and infrared (IR) active modes can indeed influence emission and absorption spectra, including photoluminescence excitation (PLE) spectra, particularly in d-d transitions observed in transition metal ions like Cr^{3+}. Raman-active modes affect the material's polarization and can couple with electronic transitions, modifying fluorescence and absorption characteristics. In doped crystals, phonon interactions with electronic states can lead to spectral shifts or additional structures. Infrared modes, associated with vibrational transitions of the crystal lattice (e.g., Cr–O stretching), can also impact d-d transitions by altering the local crystalline environment around the Cr^{3+} ion. Such lattice vibrations modify transition energies and intensities, influencing electron-phonon coupling and spectral peak positions in PLE spectra.

In our case, $GdAlO_3$ is doped with Cr^{3+}, the vibration mode at 484 cm^{-1} could be disturbed by interactions between Cr^{3+} and the crystal lattice (e_g). Which corresponds to the Raman active mode of eg symmetry in $GdAlO_3$ host crystal. The authors of this reference [26] suggested that the same vibrational frequency of 484 cm^{-1} (~60 meV) can be used to the Cr^{3+}-doped phosphors, regardless of whether the host material is an oxide or fluoride. They considered this phonon energy to correspond to the local vibrations of the $[CrO6]^{9-}$ molecule.

The experimental PLE spectrum was fitted by adjusting the parameters $E(^4T_{2g}(^4F))_{ZPL}$ and $E(^4T_{1g}(^4F))_{ZPL}$, Γ, and ΔQ. Table 1 lists the values obtained for these quantities.

The **d-d** transitions naturally lead to broad bands where asymmetry is a dominant feature. The asymmetry observed in the PLE spectrum results from several phenomena.

- The superposition of the spin-allowed quartet transition $^4A_{2g}(^4F) \rightarrow {}^4T_{2g}(^4F)$ and the spin-forbidden doublet transition $^4A_{2g}(^4F) \rightarrow {}^2E_g(^2G)$) contributes to this asymmetry. This superposition leads to interference effects, including the formation of an interference dip.

Table 1
Parameters used to simulate the PLE spectra shown in Figs. 3 and 5.

Parameter	Value
$E(^2E(^2G))_{ZPL}$	13774 cm^{-1}
$E(^4T_{2g}(^4F))_{ZPL}$	16393 cm^{-1}
Γ	5 cm^{-1}
k, ΔQ	484 cm^{-1}, 2.6
$E(^4T_{1g}(^4F))_{ZPL}$	22831 cm^{-1}
Γ	6 cm^{-1}
k, $\Delta Q'$	484 cm^{-1}, 3.82

To model spectra exhibiting such asymmetric band shapes, one effective approach involves utilizing the Fourier transform of the autocorrelation function while incorporating experimental data from both spin-multiplicity transitions. This method has been successfully applied in the case of lithium-chromium phosphate compound $Li_3Cr_2(PO_3)_4$ [27].

- Additionally, the PLE spectrum of Cr^{3+} ions in $ZnAl_2O_4$ demonstrate a slight asymetric profil [12]. This asymmetry arises from the distortions in the crystalline environment, despite, Cr^{3+} typically occupy high-symmetry crystalline site (O_h), but slightly distorted. In this case, we demonstrate the presence of the Jahn-Teller effect, which introduces further modifications to the electronic structure, contributing to the observed asymmetry.
- In addition, other effects can further enhance the d-d band. So, at low temperatures, vibrational relaxation and lattice distortions become more pronounced, contributing to the asymmetry in the d-d transitions of transition metal ions and deviating from ideal symmetry. Structural inhomogeneities and defects in the local environment of these ions also introduce additional perturbations, which, when amplified by the freezing out of lattice vibrations, result in increased broadening and asymmetry in the PLE spectra. It is evident from the spectrum that the asymmetry is negligible, allowing us to apply the autocorrelation function.

A single normal coordinate Q was used in the model owing to the characteristics of the electronic transitions, which correspond to the intra-configuration d-d excitations. The excited doublet state $^2E_g(^2G)$ and the ground $^4A_{2g}(^4F)$ (Q = 0 Å) states share the same vibrational frequency and the same position of the potential energy minimum [12]. On the other hand, the $^4T_{2g}(^4F)$, as well as the $^4T_{1g}(^4F)$ and $^4T_{1g}(^4P)$ states are shifted to longer metal-ligand bond distances, because in these cases the metal-ligand antibonding molecular orbitals are populated by d-d excitation [12]. The magnitude of the corresponding displacements ΔQ, $\Delta Q'$ is determined from the width of the $^4T_{2g}(^4F)$ and $^4T_{1g}(^4F)$ bands of the PLE experimental spectrum. The potentials (V) for the excited states $^2E_g(^2G)$, $^4T_{2g}(^4F)$, $^4T_{1g}(^4F)$ and $^4T_{1g}(^4P)$ are as follows:

$$V(^2E_g(^2G)) = \frac{1}{2}(kQ^2) + E(^2E_g(^2G))_{ZPL} \quad (3\text{-a})$$

$$V(^4T_{2g}(^4F)) = \frac{1}{2}(k(Q-\Delta Q_1)^2) + E(^4T_{2g}(^4F))_{ZPL} \quad (3\text{-b})$$

$$V(^4T_{1g}(^4F)) = \frac{1}{2}(k(Q-\Delta Q_1)^2) + E(^4T_{1g}(^4F))_{ZPL} \quad (3\text{-c})$$

$$V(^4T_{1g}(^4P)) = \frac{1}{2}(k(Q-\Delta Q_1)^2) + E(^4T_{1g}(^4P))_{ZPL} \quad (3\text{-d})$$

where $E(^4T_{2g}(^4F))_{ZPL}$, $E(^4T_{1g}(^4F))_{ZPL}$, and $E(^4T_{1g}(^4P))_{ZPL}$ are the energies of the potential minimum for the $^4T_{2g}(^4F)$, $^4T_{1g}(^4F)$, and $^4T_{1g}(^4P)$ states, respectively, and k is the Raman frequency of $GdAlO_3$ assigned to the active mode e_g (484 cm^{-1}) [13]. The diabatic potential energy profiles obtained from Equations (3a-d) and from the spectroscopic parameters shown in Table 1 are depicted in Fig. 6.

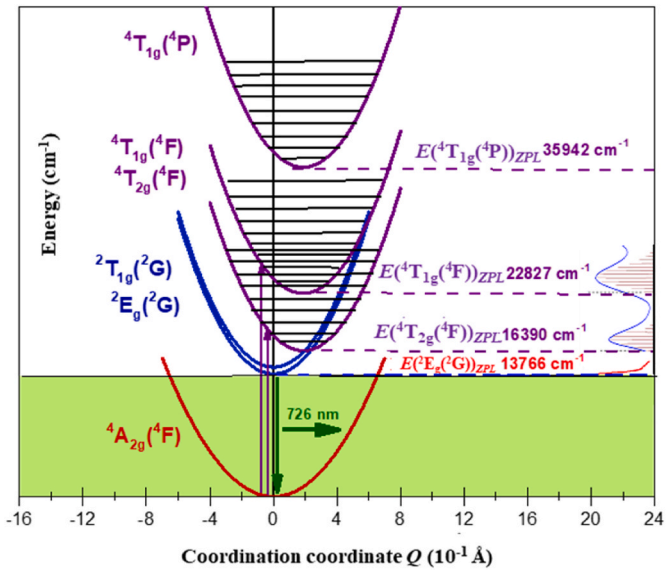

Fig. 6. Calculated diabatic potential energy profiles for $^2E_g(^2G)$, $^4T_{2g}(^4F)$, $^4T_{1g}(^4F)$ and $^4T_{1g}(^4P)$ states. The horizontal bars, shown vertically on the right side of the figure within the photoluminescence excitation (PLE) spectrum, represent the theoretical fits using Equations (1) and (2).

3.2.2. *Crystal field study of the Cr^{3+} ion in $GdAlO_3$*

The electronic structure of transition metal complexes can be explained using Crystal Field Theory (CFT). This theory has been particularly valuable for the prediction and understanding of electric, optical and magnetic properties in this type of compounds. In here one will focus on the electronic structure of Cr^{3+} ions in $GdAlO_3$: Cr^{3+} (O_h symmetry site).

The energy levels of Cr^{3+} ions can be calculated using the following total Hamiltonian [22,23,28–32]:

$$H = H_0 + H_{ee}(B,C) + H_{Trees}(\alpha_{Trees}) + H_{CF}(Dq) + H_{SO}(\zeta) \quad (4)$$

where H_0 is the configuration Hamiltonian associated with the energy of the free ion E_0, H_{ee} is the electron-electron repulsions Hamiltonian, that is a function of the Racah parameters B and C (this Hamiltonian leads to the Russell-Saunders terms ^{2S+1}L, resulting for Cr^{3+} in a 3 d^3 configuration) [33–35], H_{Trees} corresponds to the Trees correction, which depends upon the α_{Trees} fine-structure parameter and relates to the two-body orbit-orbit polarization interaction [36,37], and H_{CF} and H_{SO} represent the crystal field and the spin–orbit coupling Hamiltonians, respectively.

For octahedral symmetry (O_h), the crystal field Hamiltonian (H_{CF}), represented in the Wybourne's notation, is given by [38,39]:

$$H_{CF} = 21Dq\left[C_0^{(4)} + \sqrt{\frac{5}{14}}\left(C_0^{(4)} + C_{-4}^{(4)}\right)\right] \quad (5)$$

where D_q is the ligand field splitting due to the crystal field. The calculation of matrix elements of the Racah tensor operators C_q^k is performed through numerical methods employing Racah tensor algebraic techniques, as detailed in reference. [40]

The spin–orbit coupling Hamiltonian (H_{SO}) is a function of the ζ parameter, which expresses the degree of interaction between the electrons' spin and orbital motion.

Parametersα_{Trees} and ζcan be obtained from Equations. 6a-b [29–31]:

$$\alpha_{Trees} = N\,[4]\alpha_0 \quad (6\text{-a})$$

$$\zeta = N^2\zeta_0 \quad (6\text{-b})$$

where α_0 and ζ_0 are theα_{Trees} and ζ parameters for the free ion, and the

reduction factor N, accounts for the nephelauxetic effect, expressing the degree of covalency:

$$N^2 = \frac{1}{2}\left(\sqrt{\frac{B}{B_0}} + \sqrt{\frac{C}{C_0}}\right) \quad (7)$$

In Equation 7, B and C are the Racah parameters for the ion in the complex, while B_0 and C_0, refer to the free ion parameters. Values for B_0 and C_0, as well as α_0 and ζ_0 are shown in Table 2 [12]. The nephelauxetic effect refers to the phenomenon in which the presence of ligands in a coordination compound causes a decrease in the crystal field splitting energy or a reduction in the effective ligand field strength. It relates with how much the value of a certain coordination-related property (e.g., bond length, bond strength, etc.) varies from what would be expected in a purely ionic model due covalency in the host matrix [41]. A quantitative indicator of the degree of reduction in the studied system is given in Table 2 (see values for ratios $\beta_B = B/B_0$ and $\beta_C = C/C_0$). We will come back to this point below.

The energy values for Cr^{3+} ions in the $GdAlO_3$ perovskite are calculated theoretically using the diagonalization of the 120 × 120 matrix of the free ion eigenstates $\{|L\ S\ M_L M_S\rangle\}$ corresponding to the Hamiltonian of Equation (4). We used a specific code for diagonalization that was created in our laboratory using the Maple software and that require input of parameters B, C, Dq, α_{Trees} and ζ.

After diagonalization, the computed energies are written as functions of the B, C, Dq, α_{Trees} and ζ parameters and take the form of analytical equations. Reliable crystal-field (Dq) and Racah (B, C) parameters for Cr^{3+} ions doping $GdAlO_3$ were calculated from the experimentally measured excitation energies to the quartet excited state $^4T_{2g}(^4F)$, and the $^4T_{1g}(^4F)$ and $^2E_g(^2G)$ excited states, respectively. Equations (6) and (7) were used to derive the values of the parameters α_{Trees} and ζ. The computed energies are provided in Table 3 and are in excellent agreement with those reported by Yeung et al. [42].

The nature of the bonding for Cr^{3+} in $GdAlO_3$ can be inspected in more details in relation to the nephelauxetic effect (expressed in the value of the dimensionless h parameter in Equation (8)), specifically how the bonding between the Cr^{3+} ion and its ligands affects the value of the Racah parameter B, which as mentioned above is a measure of electron-electron repulsion within the d-orbitals of the metal ion [43].

$$h = \left[\frac{B_0 - B}{B_0 k}\right] \quad (8)$$

For oxygen hexacoordinated Cr^{3+}, in Equation (8) k is a constant with a value of 0.21 [44], so that h is 1.44. This high h value indicates a considerable impact of the ligands on the d-electron orbitals electron distribution, causing a substantial reduction in electron-electron repulsion and testifying strong ligand-metal interactions. Typically, such high values of the h parameter occur for ligands that are good electron donors or have strong π-bonding interactions with the metal center that lead to a greater delocalization of electron density, reducing the effective repulsion between electrons in the d-orbitals. This also means that the degree of delocalization is high and the electron density is shared or redistributed to a greater extent compared to a purely ionic bond, *i.e.*, the covalency is considerable.

Table 2
Optical parameters for the theoretical study of $GdAlO_3$: Cr^{3+}.

Parameter	Value
Dq	1639 cm^{-1}
B	640 cm^{-1}
C	3008 cm^{-1}
α_{Trees}	21.37 cm^{-1}
ζ	232 cm^{-1}
Dq/B	2.56
C/B	4.7
$\beta_B = B/B_0$	0.697
$\beta_C = C/C_0$	0.728
B_0[12]	918 cm^{-1}
C_0[12]	4133 cm^{-1}
α_0 [12]	30
ζ_0 [12]	275

Table 3
Experimental and calculated (with and without consideration of spin-orbit interaction) energies (cm^{-1}) of Cr^{3+} in $GdAlO_3$: Cr^{3+} (O_h symmetry site).

O_h	E_{obs}	E_{calc}	$E_{calc/SO}$
$^4A_{2g}(^4F)$	0	0	0
$^2E_g(^2G)$	13774	13766	13888 (4)
$^2T_{1g}(^2G)$		14323	14442 (4)
			14503 (2)
$^4T_{2g}(^4F)$	17699	16390	16297 (2)
			16356 (4)
			16469 (2)
			16479 (4)
$^2T_{2g}(^2G)$	–	20728	20789(4)
			20892 (2)
$^4T_{1g}(^4F)$	24390	22827	22721(4)
			22739 (2)
			22755 (4)
			22759 (2)
$^2A_{1g}(^2G)$	–	27974	28159 (2)
$^2T_{1g}(^2P)$	–	30017	30221 (2)
			30270 (4)
$^2T_{1g}(^2H)$	–	30381	30468 (2)
			30646 (4)
$^2E_g(^2H)$	–	31999	32129 (4)
$^2T_{1g}(^2H)$	–	34889	34929 (2)
			34950 (4)
$^4T_{1g}(^4P)$	–	35942	35810 (2)
			35824 (4)
			35941 (4)
			35943 (2)
$^2T_{2g}(^2H)$	–	39435	39343 (2)
			39432 (4)
$^2A_{2g}(^2F)$	–	40774	40784 (2)
$^2T_{2g}(^2D_a)$	–	46393	46650 (2)
			46760 (4)
$^2T_{2g}(^2F)$	–	47889	47921 (2)
			48041 (4)
$^2E_g(^2D_a)$	–	49024	49038 (4)
$^2T_{1g}(^2F)$	–	52672	52573 (2)
			52694 (4)
$^2T_{2g}(^2D_b)$	–	66701	66569 (4)
			66758 (2)
$^2E_g(^2D_b)$	–	69207	69252 (4)

Fig. 7 presents the Tanabe-Sugano energy-level diagram illustrating how the Dq/B ratio (local field strength) affects the electronic energy levels (expressed as *E*/B) of a Cr^{3+} (3d [3]) ion in an O_h site (C/B = 4.7), highlighting the case for Cr^{3+} (3d [3]) in $GdAlO_3$ perovskite, which corresponds to Dq/B = 2.56 and (see Table 2). The Tanabe-Sugano shows that, compared to the region Dq/B < 1.3, in the region of 1.3 < Dq/B < 2.1 the second excited state changes from $^4T_{1g}(^4F)$ to $^2E_g(^2G)$ in keeping the first excited state as being $^4T_{2g}(^4F)$. In the region of 2.1 < Dq/B < 3.3, the first excited state becomes $^2E_g(^2G)$, with the next excited states being $^2T_{1g}(^2G)$, $^4T_{2g}(^4F)$, $^2T_{2g}(^2G)$ and $^4T_{1g}(^4F)$. As mentioned, the vertical line in Fig. 7 that corresponds to the Dq/B value established from this theoretical computation represents the case of Cr^{3+} in $GdAlO_3$ perovskite.

It is interesting to note that, as shown in Fig. 6, the electronic energy of the O_h Cr^{3+} (3d [3]) $^4T_{2g}(^4F)$, $^4T_{1g}(^4F)$ and $^4T_{1g}(^4P)$ excited states is strongly dependent on the specific lattice and ligands, *via* Q. This is because the crystal-field strength Dq changes considerably with the distance between the ion and the ligands. For example, the optical transitions from the $^4A_{2g}(^4F)$ ground state to the $^2E_g(^2G)$, $^2T_{1g}(^2G)$, and $^2T_{2g}(^2G)$ states are both parity and spin forbidden. As a result, any $^2E_g(^2G)$, $^2T_{1g}(^2G)$, and $^2T_{2g}(^2G)$-related optical transitions are predicted

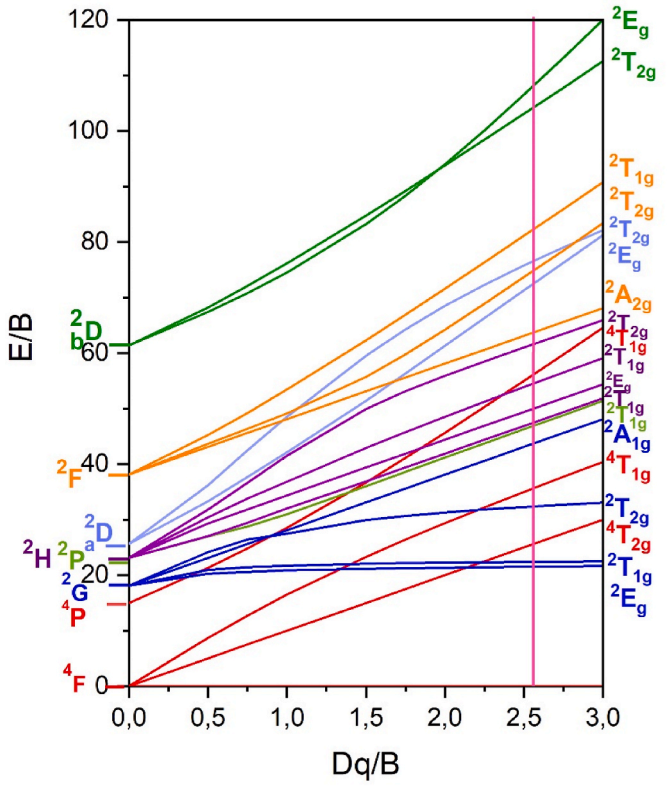

Fig. 7. Tanabe-Sugano energy-level diagram for a Cr^{3+} (3d [3]) ion in octahedral symmetry site for C/B = 4.7. The vertical line for Dq/B = 2.56 represents the case of Cr^{3+} in $GdAlO_3$.

as not observable by theory. However, the spin-orbit coupling between states of distinct multiplicity may cause the $^2E_g(^2G)$-related optical transitions to become detectable, as observed experimentally for $GdAlO_3$: Cr^{3+}. Also, the transition from $^4A_{2g}(^4F)$ to $^4T_{2g}(^4F)$ is spin-allowed, but parity-forbidden. In this case, the optical absorption/emission transitions associated with $^4T_{2g}(^4F)$ can be expected to appear as a broad band caused by interactions with a specific lattice vibrational mode, pointed out before. Experiments confirm this prediction (see Fig. 3).

3.2.3. *Luminescence life time and Gd^{3+} to Cr^{3+} energy transfer in $Gd_{0.995}Cr_{0.005}AlO_3$*

Accordingly, the PL spectrum of $GdAlO_3$:Cr^{3+} shows a decrease in the emission intensity of the Gd^{3+} ion at 698 nm and 718 nm ($^6P_j \rightarrow {}^8S_{7/2}$) compared to the emission intensity in the spectrum of pristine $GdAlO_3$ (see Fig. 4). We have also noticed also that the deep-red band at 726 nm, corresponding mostly to luminescence $^2E_g(^2G) \rightarrow {}^4A_{2g}(^4F)$ in $GdAlO_3$: Cr^{3+} is intense (Fig. 4). These observations strongly suggest significant energy transfer from Gd^{3+} ions to the dopant Cr^{3+} ions, leading to the enhancement of the luminescence intensity of the characteristic Cr^{3+} transition.

In luminescence studies, "decay time" (or lifetime) is a key parameter that describes the period during which a material continues to emit light after being excited. Typically, d-d transitions are associated with relatively short decay times, whereas luminescence resulting from charge-transfer processes often exhibits longer decay times. The decay curve for $Gd_{0.995}Cr_{0.005}AlO_3$ phosphor recorded with excitation at 377 nm and emission at the characteristic's emission transitions of $GdAlO_3$ (697 nm) are illustrated in Fig. 8. This decay curve is fitted by a double exponential decay function indicating the presence of different luminescent states or environments:

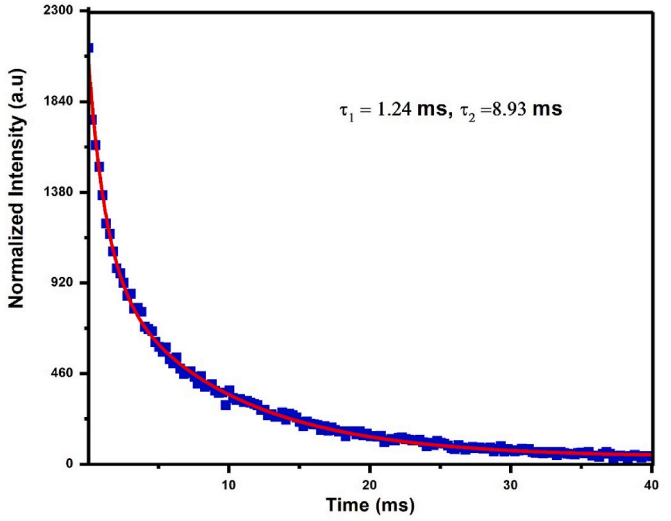

Fig. 8. Photoluminescence decay kinetics for $Gd_{0.995}Cr_{0.005}AlO_3$ phosphor collected with excitation at 377 nm and emission at the characteristic's emission transitions of $GdAlO_3$ (697 nm).

$$I(t) = A_1\, exp\left(-\frac{t}{\tau_1}\right) + A_2\, exp\left(-\frac{t}{\tau_2}\right) \quad (9)$$

I(t) is the intensity at time t, A_1 and A_2 the residual weighting parameters and τ_1 and τ_2 the decay times for different exponential components. The fitted decay times by Eq. (9) are found to be $\tau_1 = 1.24$ ms and $\tau_2 = 8.93$ ms. Thus 697 nm emission line may result from both the transition $^6P_j \rightarrow {}^8S_{7/2}$ of Gd^{3+} and also from the transition $^2E_g(^2G) \rightarrow {}^4A_{2g}(^4F)$. The electric dipole transition $^6P_j \rightarrow {}^8S_{7/2}$ gives emission at 697 nm, characterized by a low life-time value (τ_1 = 1.24 ms). The component with a higher-value life time τ_2 = 8.93 ms corresponds to emission from the spin-forbidden $^2E_g(^2G) \rightarrow {}^4A_{2g}(^4F)$ transition for Cr^{3+}. Transition metal complexes characterized by long decay times are utilized in organic light-emitting diodes and other display technologies because of their capability to sustain light emission for prolonged durations. The luminescent properties of transition metal ions, particularly those with extended decay times, are also valuable in chemical sensing and biological imaging, where time-resolved measurements can offer enhanced insights.

Based on the previously established emission lifetimes and energy levels for Cr^{3+} and Gd^{3+} ions, an energy transfer diagram is proposed for excitation at λ_{ex} = 377 nm. This diagram depicts the potential energy transfer mechanisms between the emission levels of these ions under the specified excitation wavelength.

- Just after excitation, Gd^{3+} ions become excited to the ^6I_j state then undergo non radiative relaxation to the ^6P_j state.
- Cr^{3+} ions become excited to $^4T_{1g}(^4F)$ state, then undergo non-radiative relaxation from $^4T_{1g}(^4F)$ and $^4T_{2g}(^4F)$ to the $^2E_g(^2G)$ state.
- Energy transfer occurs from ^6P_j (697 nm) state of Gd^{3+} to the $^2E_g(^2G)$ (726 nm) state.
- A strong emission at 726 nm arising from the transition $^2E_g(^2G) \rightarrow {}^4A_{2g}(^4F)$.
- A weak emissions at 697 (Gd^{3+}) arising respectively from the transitions $^6P_j \rightarrow {}^6I_{9/2}$.

The high decay time value for the transition $^2E_g(^2G) \rightarrow {}^4A_{2g}(^4F)$ and the rapidly depopulation levels of the Gd^{3+} indicates the transfer energy from Gd^{3+} to Cr^{3+}. Energy transfer in $GdAlO_3$ doped with Cr^{3+} enables the creation of solid-state lasers at specific wavelengths, highly sought after for optical communications. In radiation detectors, efficient energy transfer between Gd^{3+} and Cr^{3+} enhances the performance of GdAlO

[3]-based scintillators.

Fig. 9 presents the energy levels of Gd^{3+} and Cr^{3+}, along with an illustration of the energy transfer process between them. The high decay time value for the transition $^2E_g(^2G) \rightarrow {}^4A_{2g}(^4F)$ and the rapid depopulation levels of the Gd^{3+} indicates the transfer energy from Gd^{3+} to Cr^{3+}.

3.2.4. CIE 1931 chromaticity values for emission of $GdAlO_3:Cr^{3+}$

The CIE 1931 chromaticity values were obtained based on the emission spectra of $GdAlO_3:Cr^{3+}$ (Fig. 10). The CIE color coordinates (x, y) = (0.73372, 0.26628) reveal that the $GdAlO_3:Cr^{3+}$ phosphor emits a distinctly deep-red color, making this material suitable for the production of red light-emitting displays.

In addition, the color purity (CP) was obtained using Equation (10) [45]:

$$CP(\%) = \frac{\sqrt{(x - x_w)^2 + (y - y_w)^2}}{\sqrt{(x_d - x_w)^2 - (y_d - y_w)^2}} \times 100 \quad (10)$$

where, $(x_w, y_w) = (0.310, 0.316)$ denotes the CIE coordinates of white illumination, and $(x_d, y_d) = (0.674, 0.325)$ represents the CIE coordinates of the dominating wavelength. The results show that the color purity of the studied phosphor is virtually 100 %.

4. Conclusion

The perovskite $GdAlO_3$: Cr^{3+}, synthesized using a conventional solid-state reaction method, crystallizes in the orthorhombic Pbnm space group. In this structure, Cr^{3+} transition ions replace Al^{3+} ions within octahedral site symmetry. By modeling the photoluminescence excitation (PLE) spectrum, the zero-phonon lines (ZPL) of the observed emission and excitation transitions of the Cr^{3+} ions were determined, enabling the determination of diabatic potential energy profiles for the ground and lowest energy excited states and of crystal field parameters. The electronic structure of Cr^{3+} in $GdAlO_3$ (O_h symmetry site) has been further elucidated using a specialized code developed by S. Kammoun et al., which allowed to predict the energy levels of the Cr^{3+} ion in the studied matrix in good accordance with the experimental data. The results highlighted the significant impact of coordination on the electronic structure of Cr^{3+} ions, with a notably high nephelauxetic effect

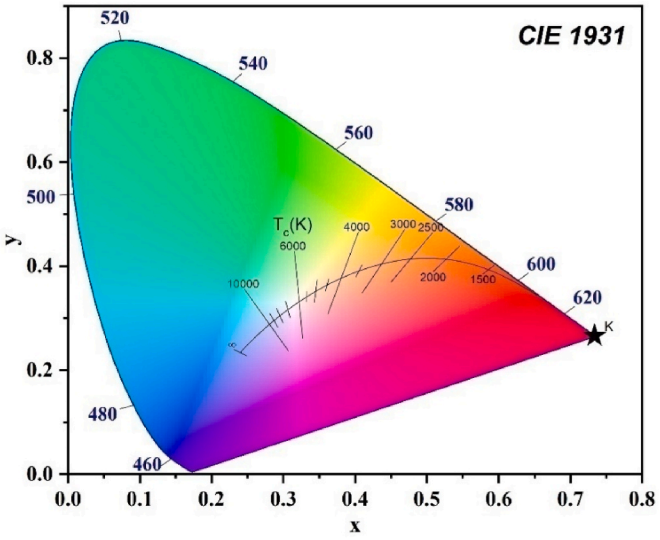

Fig. 10. The CIE diagram showing the coordinates for $GdAlO_3:Cr^{3+}$.

parameter (h = 1.44), indicating a high degree of covalency in the metal-ligand bonds.

One of the most compelling features of Cr^{3+} doping in $GdAlO_3$ is its significant impact on the material's optical properties, as demonstrated in this investigation through in-depth analyses of its photoluminescence spectra. The Cr^{3+} ions exhibit strong characteristic photoluminescence within the visible spectrum, imparting $GdAlO_3$: Cr^{3+} materials with a vibrant deep-red color. Energy transfer from Gd^{3+} to Cr^{3+} in $GdAlO_3$: Cr^{3+} was found to be significant, contributing to the enhancement of the deep-red emission of the compound attributed to the $^2E_g(^2G) \rightarrow {}^4A_{2g}(^4F)$ d-d transition of Cr^{3+}. Finally, the CIE 1931 chromaticity coordinates of the photoluminescence emission of $GdAlO_3$: Cr^{3+} were determined, positioning the emission at the boundary of the chromaticity diagram, indicative of its high color purity and potential suitability for red light-emitting display applications.

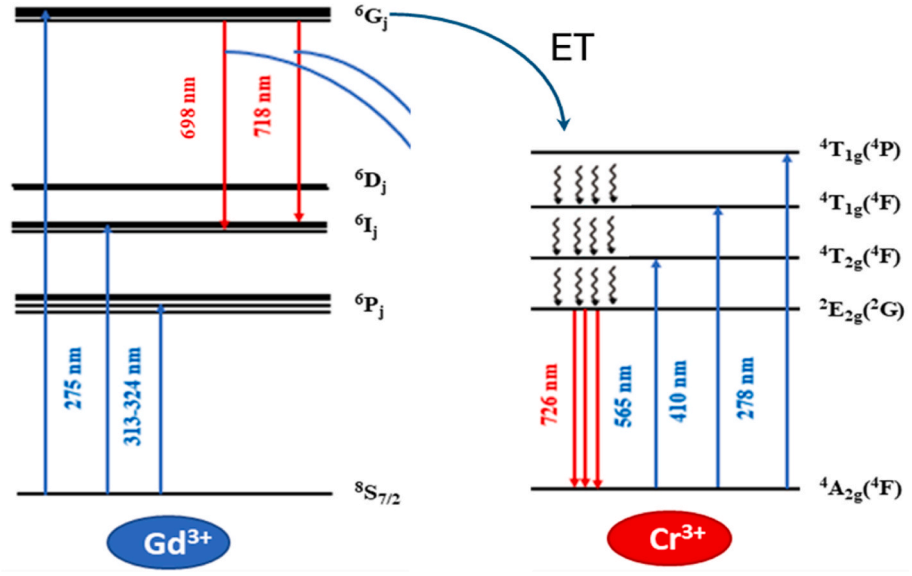

Fig. 9. Energy level diagram illustrating main transitions from Gd^{3+} to Cr^{3+} in $GaAlO_3:Cr^{3+}$, and the suggested energy transfer from Gd^{3+} to Cr^{3+} (see text).

CRediT authorship contribution statement

H. Souissi: Writing – original draft. **S. Kammoun:** Software. **E. Dhahri:** Methodology. **J. Pina:** Conceptualization. **B.F.O. Costa:** Data curation. **A.L.B. Brito:** Formal analysis. **R. Fausto:** Validation.

Declaration of competing interest

The authors declare that they have no known competing financial interests or personal relationships that could have appeared to influence the work reported in this paper.

Acknowledgements

This work was partially supported by FCT - Fundação para a Ciência e Tecnologia, I.P. through the projects UIDB/04564/2020 and UIDP/04564/2020, with DOI identifiers 10.54499/UIDB/04564/2020 and 10.54499/UIDP/04564/2020, respectively. The CQC-IMS is supported by FCT through projects UIDB/00313/2020 (DOI:10.54499/UIDB/00313/2020), UI0313P/QUI/2020 (DOI 10.54499/UIDP/00313/2020). R.F. acknowledges support from Horizon-Widera-2023-Talents-01 ERA-Chair 1011848998 Spectroscopy@IKU *"Manipulating and Characterizing Molecular Architectures: From Isolated Molecules to Molecular Crystals"*.

Data availability

Data will be made available on request.

References

[1] H. Luo, P. Dorenbos, The dual role of Cr^{3+} in trapping holes and electrons in lanthanide co-doped $GdAlO_3$ and $LaAlO_3$, J. Mater. Chem. C 6 (2018) 4977.
[2] M. Mora, A. Durygin, V. Drozd, S. Esdaille, J. Chen, S. Saxena, X. Liang, L. Vasylechko, Experimental observation of possible pressure-induced phase transformation in $GdAlO_3$ perovskite using *in situ* X-ray diffraction, Crystals 13 (2023) 1060.
[3] T. Deng, X. Jiang, Q. Zhang, Sustainably adjusting the up-conversion white-emitting luminescence properties of $GdAlO_3$: $Er^{3+}/Yb^{3+}/Tm^{3+}$ Phosphors, Front. Chem. 8 (2020) 788.
[4] J.I. Eldridge, Single fiber temperature probe configuration using anti-Stokes luminescence from Cr: $GdAlO_3$. Meas, Sci. Technol. 29 (2018) 065206.
[5] S. Adachi, Review - photoluminescence properties of Cr^{3+}-activated oxide phosphors.ECS J, Solid State Sci. Technol. 10 (2021) 026001.
[6] P. Kumar, D. Singh, I. Gupta, S. Singh, V. Kumar, Structural and luminescent characteristics of orthorhombic $GdAlO_3$: Sm^{3+} nanocrystalline materials for solid statelighting, Chem. Phys. Lett. 812 (2023) 140277.
[7] S. Idrissi, H. Labrim, L. Bahmad, A. Benyoussef, Structural, electronic, and magnetic properties of the rare earth-based solar perovskites, $GdAlO_3$, $DyAlO_3$ and $HoAlO_3$, J. Super conduct. Novel Magnet 34 (2021) 2371.
[8] R.K. Sajwan, S. Tiwari, T. Harshit, A.K. Singh, Recent progress in multicolor tuning of rare earth-doped gadolinium aluminate phosphors $GdAlO_3$, Opt. Quant. Electron. 49 (2017) 344.
[9] P. Zhang, M. Gao, R. Guo, J. Xu, Y. Wang, L. Luo, Structural and optical properties of $GdAlO_3$: Tb^{3+} crystal obtained by optical floating zone method, Optik 239 (2021) 166880.
[10] J.P. Andreeta, B.R. Jovanic, Growth and optical properties of Cr^{3+} doped $GdAlO_3$ single crystals, Mater. Res. 3 (2000) 45.
[11] P. Dorenbos, E. Bougrine, J.D. Haas, C. Eijk, M. Korzhik, Scintillation properties of $GdAlO_3$: Ce crystals, Rad. Eff. Def.Solid 135 (1995) 321.
[12] I. Elhamdi, H. Souissi, S. Kammoun, E. Dhahri, A.L.B. Brito, R. Fausto, B.F.O. Costa, Experimental determination and modeling of structural, vibrational and optical properties of the $ZnAl_{2-x}Cr_xO_4$ ($x = 0$ and 0.05) spinels, J. Lumin. 263 (2023) 119968.
[13] I. Elhamdi, F. Mselmi, S. Kammoun, E. Dhahri, A. Carvalho, P. Tavares, B.F. O. Costa, A far red emitting $ZnAl_{1.95}Cr_{0.05}O_4$ phosphor for plant growth LED applications, Dalton Trans. 52 (2023) 9301.
[14] I. Elhamdi, H. Souissi, O. Taktak, S. Kammoun, E. Dhahri, J. Pina, B.F.O. Costa, E. López-Lago, Optical characterization and defect-induced behavior in $ZnAl_{1.999}Ho_{0.001}O_4$ spinel: unraveling novel insights into structure, morphology, and spectroscopic features, Helyon 10 (2024) e29241.
[15] I. Elhamdi, H. Souissi, S. Kammoun, E. Dhahri, J. Pina, B.F.O. Costa, E. López-Lago, Comprehensive characterization and optoelectronic significance of Ho^{3+} and Cr^{3+} co-doped $ZnAl_2O_4$ spinels, Dalton Trans. 53 (2024) 7721.
[16] W.C. Hu, C.H. Kao, F.P. Yang, H.C. Jiau, K.F. Ssu, VESTA: 22nd International Conference on Software Engineering and Knowledge Engineering, vol. 2010, SEKE, 2010, p. 345.
[17] M.-H. Yuan, H.-H. Fan, H. Li, S. Lan, S.-L. Tie, Z.-M. Yang, Controlling the two-photon-induced photon cascade emission in a Gd^{3+}/Tb^{3+}-Co-doped glass for multicolor display, Sci. Rep. 6 (2016) 21091.
[18] H.C. Yang, C.Y. Li, H. He, Y. Tao, J.H. Xu, Q. Su, VUV–UV excited luminescent properties of $LnCa_4O(BO_3)_3$: RE^{3+} (Ln=Y, La, Gd; RE =Eu, Tb, Dy, Ce), J. Lumin. 118 (2006) 61.
[19] J. Li, C. Wang, J. Shi, P. Li, Z. Yu, H. Zhang, Porous $GdAlO_3$:Cr^{3+}, Sm^{3+} drug carrier for real-time long afterglow and magnetic resonance dual-mode imaging, J. Lumin. 199 (2018) 363.
[20] W.T. Carnall, H. Crosswhite, H.M. Crosswhite, Energy Level Structure and Transition Probabilities in the Spectra of the Trivalent Lanthanides in LaF_3, Office of Scientific and Technical Information (OSTI), 1978. Technical Report.
[21] A. Neffati, H. Souissi, S. Kammoun, Electronic structure of Co-doped ZnO nanorods, J. Appl. Phys. 112 (2012) 083112.
[22] O. Taktak, H. Souissi, S. Kammoun, Optical absorption properties of ZnF_2-RO-TeO_2 (R = Pb, Cd and Zn) glasses doped with chromium (III): neuhauser model and crystal field study, Opt. Mater. 113 (2021) 110682.
[23] H. Souissi, O. Taktak, S. Kammoun, Crystal field study of chromium (III) ions doped antimony phosphate glass: fano's antiresonnance and Neuhauser models, Indian J. Phys. 92 (2018) 1153.
[24] J.I. Zink, Photo-induced metal–ligand bond weakening, potential surfaces, and spectra, Coord. Chem. Rev. 211 (2001) 69.
[25] J.I. Zink, K.S.K. Shim, Molecular distortions in excited electronic states determined from electronic and resonance Raman spectroscopy, Adv. Photochem. 16 (1991) 119.
[26] S. Adachi, Review—Photoluminescence properties of Cr^{3+}-activated fluoride phosphors, ECS J. Solid State Sci. Technol. 10 (2021) 036001.
[27] H. Souissi, S. Kammoun, E. Dhahri, E.L. Lago, B.F.O. Costa, Exploring the structural and optical properties of lithium-chromium phosphate $Li_3Cr_2(PO_3)_4$, Heliyon 10 (2024) e36188.
[28] O. Maalej, O. Taktak, B. Boulard, S. Kammoun, Study with analytical equations of absorption spectra containing interference dips in fluoride glasses doped with Cr^{3+}, J. Phys. Chem. B 120 (2016) 7538.
[29] S. Kammoun, J. El Ghoul, Structural and optical investigation of Co-doped ZnO nanoparticles for nanooptoelectronic devices, J. Mater. Sci. Mater. Electron. 32 (2021) 7215.
[30] H. Souissi, S. Kammoun, Theoretical study of the electronic structure of a tetragonal chromium (III) complex, J. Lumin. 131 (2011) 2515.
[31] F. Mselmi, A. Neffati, S. Kammoun, Theoretical investigation of the cathodoluminescence spectra of Co-doped ZnO nanowires, J. Lumin. 198 (2018) 124.
[32] F. Mselmi, O. Taktak, H. Souissi, S. Kammoun, Correlation between experimental spectroscopic study and crystal-field calculations of Co^{2+} ions in α-$ZnAl_2S_4$ spinel, J. Lumin. 206 (2019) 319.
[33] S. Sugano, Y. Tanabe, H. Kamimura, Multiplets of Transition-Metal Ions in Crystals, Academic Press, New York, 1970.
[34] J.S. Griffith, The Theory of Transition-Metal Ions, Cambridge University Press, Cambridge, 1961.
[35] R.C. Powell, Physics of Solid-State Laser Materials, Springer-Verlag, Springer New York, 1998, pp. 215–233.
[36] Z.-Y. Yang, C. Rudowicz, Y.-Y. Yeung, Microscopic spin-Hamiltonian parameters and crystal field energy levels for the low C_3 symmetry Ni^{2+} centre in $LiNbO_3$ crystals, Physica B 348 (2004) 151.
[37] C. Rudowicz, Z.-Y. Yang, Y.-Y. Yeung, J. Qin, Crystal field and microscopic spin Hamiltonians approach including spin–spin and spin–other-orbit interactions for d^2 and d^8 ions at low symmetry C3 symmetry sites: V^{3+} in Al_2O_3, J. Phys. Chem. Solid. 64 (2003) 1419.
[38] D.J. Newman, B. Ng, Crystal Field Handbook, Cambridge University Press, 2000, pp. 28–36.
[39] B.G. Wybourne, Spectroscopic Properties of Rare Earths, 1th Ed., Wiley, New York, 1965, pp. 48–234.
[40] J.P. Elliott, B.R. Judd, W.A. Runciman, Energy Levels in rare-earth ions, Proc. R. Soc. London, Ser. A 240 (1957) 509.
[41] M.G. Zhao, J.A. Xu, G.R. Bai, H.S. Xie, Erratum: d-orbital theory and high-pressure effects upon the EPR spectrum of ruby, Phys. Rev. B 27 (1983) 1516.
[42] Y.Y. Yeung, C. Rudowicz, Ligand field analysis of the $3d^N$ ions at orthorhombic or higher symmetry sites, Comput. Chem. 16 (1992) 207.
[43] W. Seeber, D. Ehrt, H. Eberdorff-Heidepriem, Spectroscopic and laser properties of $Ce^{3+}/Cr^{3+}/Nd^{3+}$ co-doped fluoride phosphate and phosphate glasses, J. Non-Cryst. Solids 171 (1994) 94.
[44] C.K. Jorgensen, H. Hartmann, Absorption Spectra and Chemical Bonding in Complexes, Pergamon Press, Oxford, London, New York, Paris, 1963, p. 113.
[45] C.S. McCamy, Correlated color temperature as an explicit function of chromaticity coordinates, Color Res. Appl. 17 (1992) 142.